$\mathcal{PT}$-Symmetric Magnon Lasing and Antilasing

Xi-guang Wang,[1] Tian-xiang Lu,[2] Guang-hua Guo,[1] Jamal Berakdar,[3,*] and Hui Jing[4,5,†]
[1]*School of Physics, Central South University, Changsha 410083, China*
[2]*College of Physics and Electronic Information, Gannan Normal University, Ganzhou 341000, China*
[3]*Institut für Physik, Martin-Luther Universität Halle-Wittenberg, 06099 Halle/Saale, Germany*
[4]*College of Science, National University of Defense Technology, Changsha 410073, China*
[5]*Key Laboratory of Low-Dimensional Quantum Structures and Quantum Control of Ministry of Education, Department of Physics, Hunan Normal University, Changsha 410081, China*

(Received 16 November 2025; accepted 1 June 2026; published 6 July 2026)

A mechanism for electrically tunable $\mathcal{PT}$-symmetric magnonic lasing and antilasing is proposed along with a device consisting of a current-biased region in a magnetically ordered planar waveguide. Within the bias area, several heavy-metal wires carrying dc charge currents are periodically attached to the waveguide, generating spatially periodic spin-orbit torques that produce electrically modulated magnon gain and loss. We demonstrate that despite the nonlinear magnon dispersion, this decorated waveguide can emit a strong, single frequency magnon mode at the Bragg point (lasing) and also absorb at the same frequency phase-matched incoming coherent magnons (antilasing). In contrast to spin torque oscillators with multimode excitations driven solely by gain, the $\mathcal{PT}$-symmetric gain-loss balance stabilizes a single magnon mode operation. The underlying physics is captured by an analytical model and validated with full material and device-specific numerical simulations. We further show that the magnonic laser absorber can be electrically tuned and implemented in ring geometries and for antiferromagnetic ordering. These results establish an experimentally realistic platform where a single element functions simultaneously as a magnon laser and absorber, opening opportunities for reconfigurable non-Hermitian magnonics and integrated magnon signal processing.

DOI: 10.1103/21ts-5d39

Introduction—Magnons have been demonstrated to function as carriers of information and to enable data processing with several advantages related to their short wavelength, controllability with various external stimuli, and ready integration in (spin)electronic circuits [1–8]. A prerequisite for magnonic functionality is the ability to generate and amplify coherent magnons in magnetically active nanostructures. Our focus here is on magnon lasing and antilasing. To realize a magnon laser emitting coherent magnons, numerous studies utilized spin torque oscillators converting a dc current into coherent magnons [8–15]. In spin torque oscillators, a dc current injects a spin current into the magnetic layer exerting an antidamping torque (gain) on the local magnetization oscillations to compensate the natural oscillation loss and to amplify the magnon amplitude [9–11,16–25]. For such scheme of electrical magnon generators based on gain, the magnon coherence and single-mode purity are usually limited by multimode excitations. Electrically synchronized spin torque oscillator arrays were adopted to achieve high purity single-mode operation [26,27]. Generally, magnonic lasing, in contrast to optics, is hampered by nonlinear dispersion due to intrinsic magnetic interactions and types of magnetic ordering. Here, a qualitatively new concept is presented for ferro- and antiferromagnets to purely amplify single magnon modes in a narrow frequency range: This is achieved by a setup involving spatially inhomogeneous spin-orbit torques (SOTs) that cause periodic enhancement (gain) and decrease (loss) of magnetization oscillations. The gain and loss are balanced, resulting in a parity-time ($\mathcal{PT}$) symmetry similar to cases in optics [28–30], acoustics [31–33], electronics [34–36], and now magnonics [37–44]. It is documented that involving $\mathcal{PT}$ symmetry in laser concepts leads to better performance. For example, one can enhance the desired mode's output while suppressing others [45–47]. An interesting finding in this area is that, with fine tuning in gain and loss, the $\mathcal{PT}$-symmetry-assisted laser can both emit and absorb coherent waves, meaning the ability for lasing and antilasing [48–53]. Recently, the cavity optomagnonic system was exploited to combine $\mathcal{PT}$-symmetry laser and magnon excitation in a yttrium iron garnet sphere [54–56].

The current proposal for $\mathcal{PT}$-symmetric magnonic lasing and antilasing is realizable in a single magnetic planar waveguide (cf. Fig. 1). The system leverages the unique magnonic features such as swift manipulation via dc current or magnetic field and nonlinear magnon interaction.

*Contact author: jamal.berakdar@physik.uni-halle.de
†Contact author: jinghui@hunnu.edu.cn

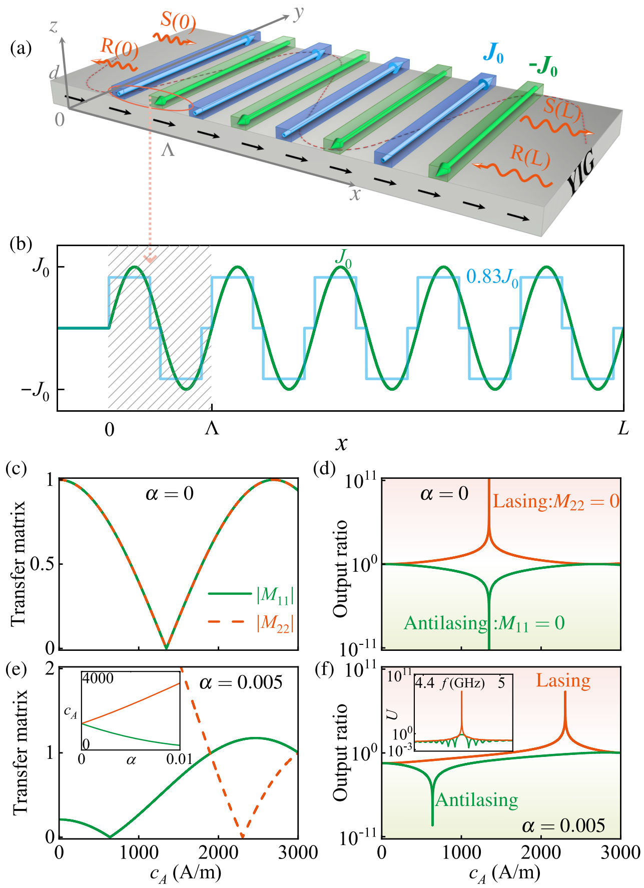

FIG. 1. (a) Schematic of a $\mathcal{PT}$-symmetry-based magnonic laser absorber. A number of electrically separated heavy-metal stripes carrying opposite charge-current densities $J_c(x)$ (flowing in y direction) are attached to a magnonic planar waveguide, generating alternating gain and loss of magnetic oscillations. (b) Spatial profiles of the sine and step functions of current density $J_c(x)$ adopted in the model. The period length $\Lambda = 100$ nm, and the total SOT region length is $L = 5000$ nm. For (c), (d) $\alpha = 0$ and (e), (f) $\alpha = 0.005$, transfer matrix elements (M_{11}, M_{22}) and output ratio U (logarithmic scale) dependence on the electric current amplitude c_A at the Bragg point $\Re[k_x] = k_p$. The inset of (e) shows the α dependent positions of $M_{11} \approx 0$ (antilasing condition) and $M_{22} \approx 0$ (lasing condition). The inset of (f) is the frequency f dependent U under the lasing and antilasing conditions. The lasing case responds to the single input excitation [$S(0) \neq 0$, $R(L) = 0$], and antilasing case means magnon excitation under two coherent inputs with $R(L)/S(0) = M_{21}$. Results follow from Eq. (4).

By reaching a critical dc current density, the regions with gain and loss emit only single-mode magnons at the Bragg point. Notably, the prevalent nonlinear effects only slightly shift the magnon frequency around the Bragg point without amplifying other modes. The structure can absorb magnons at the same frequency under two coherent inputs, achieving magnon antilaser. Such functionality is in line with the growing interest in magnetically tunable absorption [57–59]. Based on an analytical model necessary conditions are presented in this Letter for single magnon mode laser, absorber, and their manipulation mechanisms, and the influence of intrinsic Gilbert damping is analyzed. Full-fledged numerical simulations confirm the analytical prediction and enable application of the scheme to various structures, including magnetic rings and antiferromagnets, in a material- and device-specific manner. The results are potentially useful for developing new highly tunable magnonic devices merging single magnon mode oscillator and absorber.

Theoretical model—To generate the $\mathcal{PT}$-symmetric structure in a single magnonic ferromagnetic planar waveguide (along x axis), one attaches charge-current carrying heavy-metal stripes that amount to spatially varying electrical current density $J_c(x)$ flowing along the y axis, as illustrated in Fig. 1. $J_c(x)$ is perceived in the waveguide as a SOT $\mathbf{T} = \gamma c_J \mathbf{m} \times \mathbf{e}_x \times \mathbf{m}$ with the strength $c_J = \theta_{SH}(\hbar J_c / 2\mu_0 e d M_s)$. Here, M_s is the saturation magnetization, θ_{SH} is the spin-Hall angle, d is the thickness of the magnetic layer, and γ is the gyromagnetic ratio. The magnonic modes and nonlinearities are well captured by the Landau-Lifshitz-Gilbert equation [17,18,20],

$$\frac{\partial \mathbf{m}}{\partial t} = -\gamma \mathbf{m} \times \mathbf{H}_{\mathrm{eff}} + \alpha \mathbf{m} \times \frac{\partial \mathbf{m}}{\partial t} + \mathbf{T}, \tag{1}$$

where $\mathbf{m}$ is the unit vector of local magnetization, and α is the intrinsic Gilbert damping of the magnetic waveguide. The effective field $\mathbf{H}_{\mathrm{eff}} = (2A_{ex}/\mu_0 M_s)\nabla^2 \mathbf{m} + H_0 \mathbf{e}_x$ consists of the internal exchange field (with the exchange constant A_{ex}) and the external magnetic field H_0. Under the effective field, the equilibrium magnetization is in the $\mathbf{e}_x$ direction. In numerical calculations, we adopt following parameters of yttrium iron garnet: $M_s = 1.4 \times 10^5$ A/m, $A_{ex} = 3 \times 10^{-12}$ J/m, $H_0 = 1 \times 10^5$ A/m, and $\alpha = 0.005$ [60–64].

Results and discussions—We start with a $\mathcal{PT}$-symmetric magnonic laser absorber structure generated by the periodic sine function $c_J(x) = c_A \sin(2k_p x)$ with period length $\Lambda = \pi/k_p$, as shown in Fig. 1(b). The periodic region is located within $0 \leq x \leq L$, where $L = n\Lambda$ is the integer multiple of the period length. To set up an analytical model for the magnon scattering in the periodic structure, we introduce small transverse deviation $\mathbf{m}_s e^{-i\omega t}$, $\mathbf{m}_s = (0, \delta m_y, \delta m_z)$ from the equilibrium $\mathbf{m}_0 = \mathbf{e}_x$. Substituting the magnon function and defining $\psi = \delta m_y - i\delta m_z$, the linearized Landau-Lifshitz-Gilbert equation (1) is reformulated in the Helmholtz equation,

$$\psi''(x) + \left[\frac{\omega - \omega_H}{\omega_k} + i\frac{\omega_J(x)}{\omega_k}\right]\psi(x) = 0. \tag{2}$$

The following notions are introduced: $\omega_k = 2(1 - i\alpha)\gamma A_{ex}/[\mu_0 M_s(1 + \alpha^2)]$, $\omega_J(x) = (1 - i\alpha)\gamma c_J(x)/(1 + \alpha^2)$, and $\omega_H = (1 - i\alpha)\gamma H_0/(1 + \alpha^2)$. Around the nodes

$x = n\Lambda$ of the periodic potential, the electrical current term $c_J(x)$ induced gain and loss is asymmetric. Thus, the coefficient $O_H = (\omega - \omega_H)/\omega_k + i\omega_J/\omega_k$ in Eq. (2) satisfies the $\mathcal{PT}$-symmetry condition $(O_H^l)^* = O_H^r$ by neglecting α, where O_H^l and O_H^r are the coefficients in the left and right unit of the integer nodes.

In the periodic structure, we assume forward ($+x$ direction) and backward ($-x$ direction) propagating magnons to have the form $\psi(x) = S(x)e^{ik_p x} + R(x)e^{-ik_p x}$. Substituting this expression into Eq. (2), one infers the equation governing the magnons near the Bragg point ($k_x \approx k_p$),

$$\begin{aligned} -iR'(x) + \delta_k R(x) &= \xi S(x), \\ iS'(x) + \delta_k S(x) &= -\xi R(x). \end{aligned} \tag{3}$$

Solving the above equation, we extract the magnon solution at $x = L$ in the form of $[S(L), R(L)]^T = \hat{M}[S(0), R(0)]^T$, and the transfer matrix $\hat{M}$ is

$$\hat{M} = \begin{pmatrix} \cos(\beta L) + \frac{i\delta_k}{\beta}\sin(\beta L) & \frac{i\xi}{\beta}\sin(\beta L) \\ \frac{i\xi}{\beta}\sin(\beta L) & \cos(\beta L) - \frac{i\delta_k}{\beta}\sin(\beta L) \end{pmatrix}. \tag{4}$$

Here, $\omega_{JA} = (1 - i\alpha)\gamma c_A/(1 + \alpha^2)$, $\xi = \omega_{JA}/4\omega_k k_p$, $\delta_k = k_x - k_p$, $\beta = \sqrt{\delta_k^2 + \xi^2}$, and the magnon wave vector $k_x = \sqrt{(\omega - \omega_H)/\omega_k}$. From the transfer matrix element, the left and right (l/r) transmission and reflection coefficients are determined as $t_l = t_r = 1/M_{22}$, $r_l = -M_{21}/M_{22}$, and $r_r = M_{12}/M_{22}$, where the coefficients correspond to $t_l = S(L)/S(0)$, $t_r = R(0)/R(L)$, $r_l = R(0)/S(0)$, and $r_r = S(L)/R(L)$.

To achieve a magnonic laser with strong outputs $[R(0), S(L)]$ under small inputs $[R(L), S(0)]$, the element $M_{22} = 0$ is required. If we neglect α, the $\mathcal{PT}$-symmetric scattering potential yields $M_{11} = M_{22}^* = 0$. Assuming two coherent magnon inputs with amplitude and phase defined by $R(L) = M_{21}S(0)$, the output solution becomes $R(0) = S(L) = 0$, representing a perfect absorber without any reflection, i.e., antilasing. Such amplification and absorption properties make the scattering potential behave as both a magnonic laser and perfect absorber. Our numerical results in Fig. 1(c) validate these features. The lasing and antilasing conditions for $M_{11,22} = 0$ only can be reached at the Bragg point $\Re[k_x] = k_p$ when magnon frequency $f_B = \omega/(2\pi) = 4.701$ GHz and electric current amplitude $c_A = 1346$ A/m. Here, the corresponding Bragg frequency f_B is obtained from the dispersion $\omega = \omega_k k_x^2 + \omega_H$. In Fig. 1(d). we also calculate the output ratio U of total outgoing magnon intensity $[R^2(0) + S^2(L)]$ to the incoming magnon intensity $[R^2(L) + S^2(0)]$, $U = [R^2(0) + S^2(L)]/[R^2(L) + S^2(0)]$. $U > 1$ represents the magnon amplification, and $U = 0$ means perfect absorption. For the single input $[S(0) \neq 0,\ R(L) = 0]$, the output U admits very large value as the laser condition is approached. Injecting the second coherent signal $R(L) = M_{21}S(0)$, the behavior of U is obviously changed to perfect absorption at the same c_A with a dip of $U \to 0$.

In a realistic case, the influence of finite Gilbert damping must be included. See Figs. 1(e) and 1(f) with $\alpha = 0.005$, the damping-induced additional magnonic loss increases the amplitude c_A of the lasing condition $M_{22} \to 0$, while antilasing condition $M_{11} \to 0$ related c_A becomes smaller. The separation between the lasing and antilasing conditions increases with α, as proved by the inset of Fig. 1(e). Still, the output ratio $U \gg 1$ reaches large value at the lasing condition $c_A = 2305$ A/m under single input [red curve in Fig. 1(f)]. The frequency dependent U further proves that the laser is limited at the Bragg point with $f = 4.701$ GHz; see the inset of Fig. 1(f). For the antilasing at $c_A = 638$ A/m, a very small dip in U is realized by two coherent injected inputs $R(L) = M_{21}S(0)$. Noteworthy, although the antilasing condition is not satisfied at the lasing c_A, we find the ratio $U = 0.67$ is still a small value under two inputs $R(L) = M_{21}S(0)$. Such coherent injections can be realized by combining magnon power divider and delay line or phase shifter. Thus, depending on the injected magnon inputs and the current density c_A, the periodic structure can either amplify or absorb the input magnons.

The above consideration of coupled modes of $S(x)e^{ik_p x}$ and $R(x)e^{-ik_p x}$ does not include the time varying component. The laser-induced magnon amplification process requires sufficient duration. To account for time effect, we substitute $[S(x,t)e^{ik_p x} + R(x,t)e^{-ik_p x}]e^{-i\omega t}$ into Eq. (1). Combining Eq. (4), we assume the solution profile follows $[S(t) + R(t)]e^{i\beta x}$, and the magnon attenuation time is extracted from the real component of $\tau = 2i\omega_k \delta_k k_p + \sqrt{\omega_{JA}^2/4 - 4\omega_k^2 \beta^2 k_p^2}$. Using the value of β at the laser condition with the critical c_A, the real component $\Re[\tau] = 0$ indicates unattenuated magnons, and above the laser critical value there are positive $\Re[\tau] > 0$ and amplifying magnons. Such features indicate that, instead of requiring a specific c_A, the predicated magnon laser mechanism always works for c_A above the critical value. The conclusion is tested by the following full wave numerical simulation with Eq. (1).

In the numerical simulations, we adopt the step function of $c_J(x)$ [Fig. 1(b)] to generate the spatially varying gain and loss. The setting is more close to the realistic structure consisting several independent charge-carrying stripes. Simulations are done for a 2 nm × 1 μm × 20 nm unit cell covering the total waveguide size of 30 μm × 1 μm × 20 nm, and Eq. (1) is numerically solved by a finite difference method. In a single period of

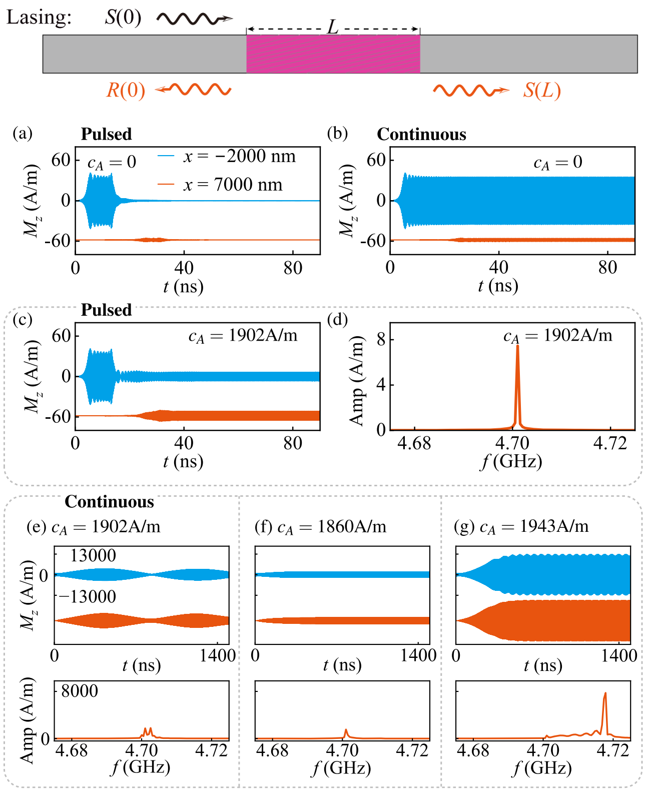

FIG. 2. Top panel is the schematic for magnon lasing with single input $S(0) \neq 0$. The magnon outputs are detected as time-dependent $M_z(t)$ at left side $x = -2000$ nm [blue curve, related to $R(0)$] and right side $x = 7000$ nm [red curve, related to $S(L)$]. The red curves are in the same range with blue curves, which are intentionally offset for clarity. Under different c_A, magnon outputs are excited by a microwave field $\mathbf{h} = h_0 \sin(2\pi f t)\mathbf{z}$ lasting 10 ns [(a) and (c)] and continuously [(b) and (e)–(g)], where frequency $f = 4.701$ GHz and amplitude $h_0 = 1000$ A/m is localized at left side $x = -4000$ nm. Frequency spectra are obtained from the laser-induced long lasting oscillation. These results are obtained from micromagnetic simulations with Eq. (1), where the laser region realized by step-type function is limited in $0 \leq x \leq 5000$ nm with period $\Lambda = 100$ nm.

$c_J(0 < x \leq \Lambda)$, the step function is $c_J(0 < x \leq 2\Lambda/5) = c_A$, $c_J(\Lambda/2 < x \leq 9\Lambda/10) = -c_A$. When its amplitude is 0.825 times c_A of sine function, the step function has the same component with the sine function at k_p in the wave vector space. As proved by Figs. 2(a) and 2(c), for the laser condition $c_A = 0.825 \times 2305 = 1902$ A/m, the injected magnon pulse (with frequency 4.701 GHz) is sustained for a long time without decaying. Without SOT ($c_A = 0$), the magnon pulse is swiftly damped. With continuous magnon injection for a long enough duration (say 300 ns) a strong magnon amplification is achieved; see Figs. 2(b) and 2(e).

Compared to optical laser absorbers [48–52], our magnonic lasing scheme differs in several qualitative ways. First, intrinsic Gilbert damping lifts the exact coincidence between the lasing and antilasing conditions, allowing for an electrically selectable magnon source or sink. Second, once the drive exceeds the lasing threshold, the coherent amplification persists over a broad range of current density, whereas the optical laser absorber generally requires fine tuning of gain and loss. Third, for the magnetic system, the amplified magnons may well enter the nonlinear regime with frequency shift, as discussed in what follows. For large magnon amplitude one enters the magnonic nonlinear regime where two very close frequencies (4.701 and 4.703 GHz) are simultaneously generated, and thus beating with long period is observed; see Fig. 2(e). Adopting a slightly smaller $c_A = 1860$ A/m in Fig. 2(f), the SOT-induced magnon enhancement becomes weaker, and the nonlinear effect is suppressed, where only 4.701 GHz is left. As for a larger $c_A = 1943$ A/m above the critical value, a further larger magnon amplitude is excited, and the main peak appears at 4.718 GHz; see Fig. 2(g). In this case, as $\Re[\tau] > 0$, the magnon amplitude is still continuously amplified even under a short pulse excitation and one obtains similar curves (not shown here). To explain the frequency shift in the nonlinear lasing regime, we extend the theoretical model to include the large amplitude magnon nonlinearity; see Supplemental Material (SM) [65]. In this regime, the longitudinal component m_x is reduced and spatially modulated, which is described by an effective equilibrium $\mathbf{m}_0 = l(x)\mathbf{e}_x$ with $l(x) < 1$. Nonlinearity affects the transfer matrix coefficients so that the lasing condition $M_{22} \to 0$ is satisfied at the shifted frequency. Two competing contributions control the frequency shift: (i) the spatial variation of $l(x)$ slightly shifts the lasing wave vector above the Bragg point, $\Re[k_x] > k_p$, and increases the lasing frequency; (ii) the reduced m_x decreases ω_k and lowers the dispersion frequency. Their combined effect causes the upward frequency shift.

The above $\mathcal{PT}$-symmetric magnon laser has the advantage of selectively amplifying the magnon mode at the Bragg point with quite narrow bandwidth (even in the nonlinear regime), while other magnon modes remain unamplified. If we introduce a pure gain (say $c_J \geq 668$ A/m) on the whole sample to compensate the intrinsic magnon damping at Bragg point, magnon modes with smaller frequencies are all amplified, causing multimode excitations. Also, the local magnetization is soon reversed and the magnons are damped. To sustain the magnetization oscillation and amplify magnons, a tilt angle between the electric polarization and equilibrium magnetization is usually required, while the mode selection is still challenging [22–25]. Here, the $\mathcal{PT}$-symmetric magnon laser avoids such limitations.

Adding other coherent magnon injection to the same structure, simulation results in Fig. 3 evidence antilasing under a different c_A. Without SOT ($c_A = 0$), the interference between two coherent magnon injections causes amplitude fluctuation in Fig. 3(a), where its spatial profile is affected by the magnon decaying. At the antilasing

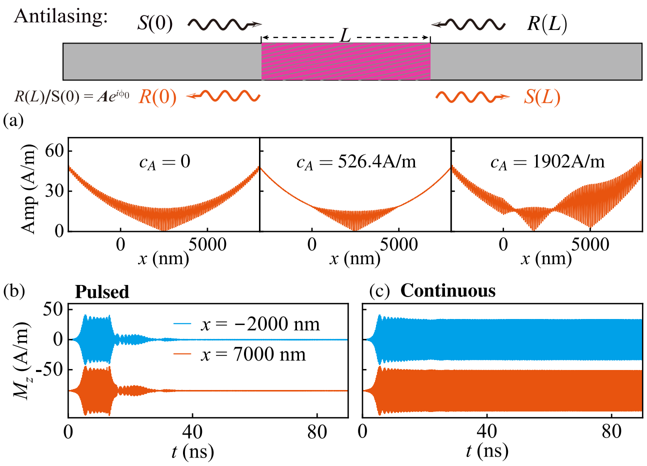

FIG. 3. Top panel is the schematic for magnon antilasing with two coherent inputs $R(L) = S(0)Ae^{i\phi_0}$. In the micromagnetic simulation with step-type electric current region in $0 \le x \le 5000$ nm, we apply two microwave fields $\mathbf{h}_1 = h_0 \sin(2\pi f t)\mathbf{z}$ (at $x = -4000$ nm) and $\mathbf{h}_2 = Ah_0 \sin(2\pi f t + \phi_0)\mathbf{z}$ (at $x = 9000$ nm) to realize the inputs. Here, $A = 1$ and $\phi_0 = -1.26$ rad are used to approach the absorber condition, $f = 4.701$ GHz and $h_0 = 1000$ A/m. (a) The spatial profiles of M_z oscillation amplitude under different c_A. (b),(c) At the critical value $c_A = 1902$ A/m, the time-dependent $M_z(t)$ profiles exited by (b) 10 ns pulsed and (c) continuous microwave fields, where the red curves with $|M_z| < 50$ A/m are intentionally offset for clarity.

condition $c_A = 0.825 \times 638 = 526.4$ A/m, the injected magnons are absorbed in the region of $0 \le x \le 5000$ nm, and the amplitude fluctuation outside the electric current region is completely erased. Notably, since the step function differs from the sine function, the phase $\phi_0 = -1.26$ rad is different from analytical estimation while the amplitude ratio $A = 1.0$ still follows $|M_{21}| = 1$. Switching to the laser condition $c_A = 1902$ A/m, two persisting coherent magnon injections totally suppress the laser amplification, while there are still clear reflections. Such observation agrees with above theoretical estimations, where $U = 0.67$ is found. As the analytical M_{21} here is identical to the antilasing condition, $A = 1$ and $\phi_0 = -1.26$ rad are still applicable. Furthermore, Figs. 3(b) and 3(c) show the time-dependent results for the magnon amplitude under pulsed and continuous excitation, and indeed the magnon amplification is completely suppressed. We also considered different A and ϕ_0, and except for the above condition the magnon laser function can be fully resumed.

To tune the magnon lasing and antilasing frequency, a different periodic length Λ can be set to change the Bragg point position. As an example, with $\Lambda = 500$ nm and $L = 1000$ nm, the laser absorber for magnon frequency 3.56 GHz is achieved (for details, see SM [65]). For such setting, only four separated charge-carrying stripes are enough, validating the effectiveness of the simpler structure

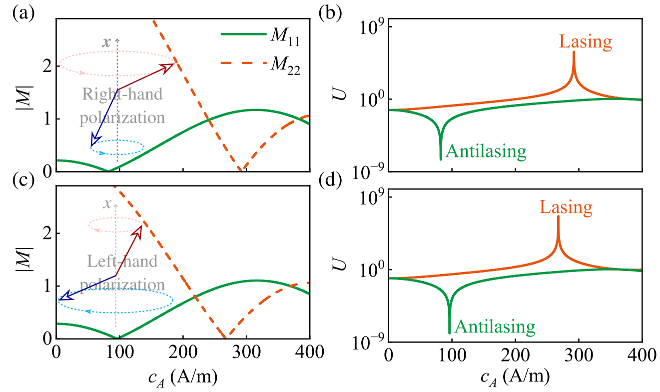

FIG. 4. For the antiferromagnetic layer with periodic SOT having $\Lambda = 50$ nm and $L = 2000$ nm, dependence of M_{11}, M_{22}, and U (logarithmic scale) on the electric current amplitude c_A for right-hand [(a), (b) frequency $\Re[\omega_+]/2\pi = 0.296$ THz] and left-hand (c) and (d), frequency $\Re[\omega_-]/2\pi = -0.24$ THz) polarized magnons. Red and blue arrows represent the two sublattice magnetizations $\mathbf{m}_1$ and $\mathbf{m}_2$. Material parameters for MnF_2 are used in the calculations: $\omega_E = 9.3$ THz, $\omega_A = 0.15$ THz, $\omega_H = 0.176$ THz, $\alpha = 2 \times 10^{-5}$, and $a = 4.1$ Å.

for the magnon laser absorber. Alternatively, we suggest to change the Bragg period by rearranging the electric current density profile in the charge-carrying stripes or adjusting the external magnetic field, which highlights the electrical or magnetic tunability of the magnon laser frequency. Furthermore, we prove that the magnon laser mechanism works for a ring geometry, and thermal magnons near the Bragg point can be selectively amplified at finite temperature, as detailed in SM [65].

The lasing and antilasing mechanism is operational for antiferromagnets, enabling selective excitation of two circularly polarized magnon modes ($\omega_\pm$) in the THz range. Using the antiferromagnetic (AFM) model detailed in SM [65], we deduce the transfer matrix in the form of Eq. (4) with the substitutions $\beta \to \beta_{\mathrm{AFM}} = \sqrt{\delta_k^2 + \xi_{\mathrm{AFM}}^2}$ and $\xi \to \xi_{\mathrm{AFM}} = [A_n J_n / 2k_p (k_a^2 - k_p^2)]$. Here, $A_n = (\omega_A/\omega_E + 1)k_a^2$, $J_n = k_a^2 \gamma c_A / (\omega_E)$, ω_E is the exchange frequency, ω_A is the anisotropy frequency with easy-axis along $\mathbf{e}_x$, ω_H represents the external magnetic field along x, $k_a = 2/a$, and a is the unit cell length. The AFM magnon wave vector k_x is determined from the dispersion relation $\omega_\pm - \omega_H = \pm\{(\omega_E k_a^2 k_x^2 + \omega_A - i\alpha\omega)(2\omega_E + \omega_A - \omega_E k_a^2 k_x^2 - i\alpha\omega)\}^{1/2}$. When $\omega_H = 0$, the two oppositely polarized magnon branches are degenerate, and the corresponding transfer matrices are identical, so opposite magnons are transmitted equally. Applying a finite field ($\omega_H \neq 0$) lifts the degeneracy, and at the same Bragg point wave vector k_p opposite magnons with unequal eigenfrequencies satisfy the lasing ($M_{22} = 0$) and antilasing ($M_{11} = 0$) conditions at different current densities. As demonstrated by Fig. 4 with a magnetic field in the $+\mathbf{e}_x$ direction, the left-hand magnon mode reaches lasing at $c_A = 268$ A/m, below the right-hand magnon threshold $c_A = 292$ A/m. Thus, choosing c_A in this window enables selective amplification of the left-hand magnon at frequency 0.24 THz. Furthermore, as the antilasing condition also splits, it is possible to selectively absorb one of the two opposite magnon modes.

Conclusions—A $\mathcal{PT}$-symmetry-based mechanism for magnon lasing and antilasing is proposed for ferro- and antiferromagnets in different geometries and for the linear and nonlinear regimes. The device is solely driven by dc currents that generate a controlled, periodically modulated gain-loss landscape implementing non-Hermitian magnon dynamics. Analytical modeling uncovers the essential physics complemented with full numerical simulations that confirm single magnon mode amplification at the Bragg point, absorption for coherent inputs at the lasing frequency, and continuous electrical tunability of emission frequency and output level. Systematic studies over current density, geometric length, and damping provide practical guidelines for device realization. The operating principle naturally extends to planar waveguide and ring geometries, where the waveguide enables on-chip integration and the ring supports stable single-mode operation. The active region also amplifies thermal magnons, pointing to low-bias startup and potential noise-shaping strategy. These results provide a clear pathway toward electrically programmable magnonic sources, sinks, and amplifiers within a single, compact component.

Acknowledgments—This work was supported by Quantum Science and Technology-National Science and Technology Major Project (Grant No. 2024ZD0301000), the National Natural Science Foundation of China (Grants No. T2495212, No. 12174452, No. 12274469, No. 12074437, No. 11935006, No. 12421005, and No. 12565001), DFG under Project No. 465098690, the National Key R&D Program (Grant No. 2024YFE0102400), the Hunan Major Sci-Tech Program (Grant No. 2023ZJ1010), and the Natural Science Foundation of Hunan Province of China (Grants No. 2025JJ20005 and No. 2022JJ20050).

Data availability—The data that support the findings of this article are openly available [70].

[1] A. V. Chumak, V. I. Vasyuchka, A. A. Serga, and B. Hillebrands, Magnon spintronics, Nat. Phys. **11**, 453 (2015).

[2] V. E. Demidov, S. Urazhdin, A. Anane, V. Cros, and S. O. Demokritov, Spin–orbit-torque magnonics, J. Appl. Phys. **127**, 170901 (2020).

[3] P. Pirro, V. I. Vasyuchka, A. A. Serga, and B. Hillebrands, Advances in coherent magnonics, Nat. Rev. Mater. **6**, 1114 (2021).

[4] V. V. Kruglyak, S. O. Demokritov, and D. Grundler, Magnonics, J. Phys. D **43**, 264001 (2010).

[5] A. A. Serga, A. V. Chumak, and B. Hillebrands, YIG magnonics, J. Phys. D **43**, 264002 (2010).

[6] K. Vogt, F. Y. Fradin, J. E. Pearson, T. Sebastian, S. D. Bader, B. Hillebrands, A. Hoffmann, and H. Schultheiss, Realization of a spin-wave multiplexer, Nat. Commun. **5**, 3727 (2014).

[7] A. V. Chumak, A. A. Serga, and B. Hillebrands, Magnon transistor for all-magnon data processing, Nat. Commun. **5**, 4700 (2014).

[8] M. Tsoi, A. G. M. Jansen, J. Bass, W.-C. Chiang, V. Tsoi, and P. Wyder, Generation and detection of phase-coherent current-driven magnons in magnetic multilayers, Nature (London) **406**, 46 (2000).

[9] Y. Kajiwara, K. Harii, S. Takahashi, J. Ohe, K. Uchida, M. Mizuguchi, H. Umezawa, H. Kawai, K. Ando, K. Takanashi, S. Maekawa, and E. Saitoh, Transmission of electrical signals by spin-wave interconversion in a magnetic insulator, Nature (London) **464**, 262 (2010).

[10] H. Merbouche, B. Divinskiy, D. Gouéré, R. Lebrun, A. El Kanj, V. Cros, P. Bortolotti, A. Anane, S. O. Demokritov, and V. E. Demidov, True amplification of spin waves in magnonic nano-waveguides, Nat. Commun. **15**, 1560 (2024).

[11] M. Collet, X. de Milly, O. d'Allivy Kelly, V. V. Naletov, R. Bernard, P. Bortolotti, J. Ben Youssef, V. E. Demidov, S. O. Demokritov, J. L. Prieto, M. Muñoz, V. Cros, A. Anane, G. de Loubens, and O. Klein, Generation of coherent spin-wave modes in yttrium iron garnet microdiscs by spin-orbit torque, Nat. Commun. **7**, 10377 (2016).

[12] D. Marković, N. Leroux, A. Mizrahi, J. Trastoy, V. Cros, P. Bortolotti, L. Martins, A. Jenkins, R. Ferreira, and J. Grollier, Detection of the microwave emission from a spin-torque oscillator by a spin diode, Phys. Rev. Appl. **13**, 044050 (2020).

[13] V. E. Demidov, S. Urazhdin, and S. O. Demokritov, Direct observation and mapping of spin waves emitted by spin-torque nano-oscillators, Nat. Mater. **9**, 984 (2010).

[14] Z. Duan, A. Smith, L. Yang, B. Youngblood, J. Lindner, V. E. Demidov, S. O. Demokritov, and I. N. Krivorotov, Nanowire spin torque oscillator driven by spin orbit torques, Nat. Commun. **5**, 5616 (2014).

[15] V. E. Demidov, S. Urazhdin, G. de Loubens, O. Klein, V. Cros, A. Anane, and S. O. Demokritov, Magnetization oscillations and waves driven by pure spin currents, Phys. Rep. **673**, 1 (2017).

[16] I. N. Krivorotov, N. C. Emley, J. C. Sankey, S. I. Kiselev, D. C. Ralph, and R. A. Buhrman, Time-domain measurements of nanomagnet dynamics driven by spin-transfer torques, Science **307**, 228 (2005).

[17] A. Hoffmann, Spin hall effects in metals, IEEE Trans. Magn. **49**, 5172 (2013).

[18] K. Garello, I. M. Miron, C. O. Avci, F. Freimuth, Y. Mokrousov, S. Blügel, S. Auffret, O. Boulle, G. Gaudin, and P. Gambardella, Symmetry and magnitude of spin-orbit torques in ferromagnetic heterostructures, Nat. Nanotechnol. **8**, 587 (2013).

[19] R. H. Liu, W. L. Lim, and S. Urazhdin, Spectral characteristics of the microwave emission by the spin Hall nano-oscillator, Phys. Rev. Lett. **110**, 147601 (2013).

[20] J. Sinova, S. O. Valenzuela, J. Wunderlich, C. H. Back, and T. Jungwirth, Spin Hall effects, Rev. Mod. Phys. **87**, 1213 (2015).

[21] A. Manchon, J. Železný, I. M. Miron, T. Jungwirth, J. Sinova, A. Thiaville, K. Garello, and P. Gambardella, Current-induced spin-orbit torques in ferromagnetic and antiferromagnetic systems, Rev. Mod. Phys. **91**, 035004 (2019).

[22] M. Haidar, A. A. Awad, M. Dvornik, R. Khymyn, A. Houshang, and J. Åkerman, A single layer spin-orbit torque nano-oscillator, Nat. Commun. **10**, 2362 (2019).

[23] H. Fulara, M. Zahedinejad, R. Khymyn, A. A. Awad, S. Muralidhar, M. Dvornik, and J. Åkerman, Spin-orbit torque-driven propagating spin waves, Sci. Adv. **5**, eaax8467 (2019).

[24] D. Houssameddine, U. Ebels, B. Delaët, B. Rodmacq, I. Firastrau, F. Ponthenier, M. Brunet, C. Thirion, J.-P. Michel, L. Prejbeanu-Buda, M.-C. Cyrille, O. Redon, and B. Dieny, Spin-torque oscillator using a perpendicular polarizer and a planar free layer, Nat. Mater. **6**, 447 (2007).

[25] S. Kaka, M. R. Pufall, W. H. Rippard, T. J. Silva, S. E. Russek, and J. A. Katine, Mutual phase-locking of microwave spin torque nano-oscillators, Nature (London) **437**, 389 (2005).

[26] R. Lebrun, S. Tsunegi, P. Bortolotti, H. Kubota, A. S. Jenkins, M. Romera, K. Yakushiji, A. Fukushima, J. Grollier, S. Yuasa, and V. Cros, Mutual synchronization of spin torque nano-oscillators through a long-range and tunable electrical coupling scheme, Nat. Commun. **8**, 15825 (2017).

[27] R. Sharma, R. Mishra, T. Ngo, Y.-X. Guo, S. Fukami, H. Sato, H. Ohno, and H. Yang, Electrically connected spin-torque oscillators array for 2.4 GHz wifi band transmission and energy harvesting, Nat. Commun. **12**, 2924 (2021).

[28] L. Feng, R. El-Ganainy, and L. Ge, Non-Hermitian photonics based on parity–time symmetry, Nat. Photonics **11**, 752 (2017).

[29] A. Guo, G. J. Salamo, D. Duchesne, R. Morandotti, M. Volatier-Ravat, V. Aimez, G. A. Siviloglou, and D. N. Christodoulides, Observation of $\mathcal{PT}$-symmetry breaking in complex optical potentials, Phys. Rev. Lett. **103**, 093902 (2009).

[30] C. E. Rüter, K. G. Makris, R. El-Ganainy, D. N. Christodoulides, M. Segev, and D. Kip, Observation of parity–time symmetry in optics, Nat. Phys. **6**, 192 (2010).

[31] X. Zhu, H. Ramezani, C. Shi, J. Zhu, and X. Zhang, $\mathcal{PT}$-symmetric acoustics, Phys. Rev. X **4**, 031042 (2014).

[32] C. Shi, M. Dubois, Y. Chen, L. Cheng, H. Ramezani, Y. Wang, and X. Zhang, Accessing the exceptional points of parity-time symmetric acoustics, Nat. Commun. **7**, 11110 (2016).

[33] R. Fleury, D. Sounas, and A. Alù, An invisible acoustic sensor based on parity-time symmetry, Nat. Commun. **6**, 5905 (2015).

[34] J. Schindler, A. Li, M. C. Zheng, F. M. Ellis, and T. Kottos, Experimental study of active LRC circuits with $\mathcal{PT}$ symmetries, Phys. Rev. A **84**, 040101 (2011).

[35] S. Assawaworrarit, X. Yu, and S. Fan, Robust wireless power transfer using a nonlinear parity-time-symmetric circuit, Nature (London) **546**, 387 (2017).

[36] P.-Y. Chen, M. Sakhdari, M. Hajizadegan, Q. Cui, M. M.-C. Cheng, R. El-Ganainy, and A. Alù, Generalized parity-time symmetry condition for enhanced sensor telemetry, Natl. Electron. Rev. **1**, 297 (2018).

[37] X.-g. Wang, G.-h. Guo, and J. Berakdar, Steering magnonic dynamics and permeability at exceptional points in a parity–time symmetric waveguide, Nat. Commun. **11**, 5663 (2020).

[38] X.-g. Wang, G.-h. Guo, and J. Berakdar, Enhanced sensitivity at magnetic high-order exceptional points and topological energy transfer in magnonic planar waveguides, Phys. Rev. Appl. **15**, 034050 (2021).

[39] A. V. Sadovnikov, A. A. Zyablovsky, A. V. Dorofeenko, and S. A. Nikitov, Exceptional-point phase transition in coupled magnonic waveguides, Phys. Rev. Appl. **18**, 024073 (2022).

[40] J. M. Lee, T. Kottos, and B. Shapiro, Macroscopic magnetic structures with balanced gain and loss, Phys. Rev. B **91**, 094416 (2015).

[41] H. Liu, D. Sun, C. Zhang, M. Groesbeck, R. Mclaughlin, and Z. V. Vardeny, Observation of exceptional points in magnonic parity-time symmetry devices, Sci. Adv. **5**, eaax9144 (2019).

[42] O. Temnaya, A. Safin, D. Kalyabin, and S. Nikitov, Parity-time symmetry in planar coupled magnonic heterostructures, Phys. Rev. Appl. **18**, 014003 (2022).

[43] Y. Yang, Y.-P. Wang, J. W. Rao, Y. S. Gui, B. M. Yao, W. Lu, and C.-M. Hu, Unconventional singularity in anti-parity-time symmetric cavity magnonics, Phys. Rev. Lett. **125**, 147202 (2020).

[44] S. Wittrock, S. Perna, R. Lebrun, K. Ho, R. Dutra, R. Ferreira, P. Bortolotti, C. Serpico, and V. Cros, Non-hermiticity in spintronics: Oscillation death in coupled spintronic nano-oscillators through emerging exceptional points, Nat. Commun. **15**, 971 (2024).

[45] H. Hodaei, M.-A. Miri, M. Heinrich, D. N. Christodoulides, and M. Khajavikhan, Parity-time–symmetric microring lasers, Science **346**, 975 (2014).

[46] H. Jing, S. K. Özdemir, X.-Y. Lü, J. Zhang, L. Yang, and F. Nori, $\mathcal{PT}$-symmetric phonon laser, Phys. Rev. Lett. **113**, 053604 (2014).

[47] J. Zhang, B. Peng, Ş. K. Özdemir, K. Pichler, D. O. Krimer, G. Zhao, F. Nori, Y.-x. Liu, S. Rotter, and L. Yang, A phonon laser operating at an exceptional point, Nat. Photonics **12**, 479 (2018).

[48] S. Longhi, $\mathcal{PT}$-symmetric laser absorber, Phys. Rev. A **82**, 031801 (2010).

[49] M. Yang, Q. Zhong, Z. Ye, S. K. Özdemir, M. Farhat, R. El-Ganainy, and P.-Y. Chen, Experimental observation of coherent-perfect-absorber and laser points in anti-PT symmetry, Phys. Rev. A **110**, 033504 (2024).

[50] Z. J. Wong, Y.-L. Xu, J. Kim, K. O'Brien, Y. Wang, L. Feng, and X. Zhang, Lasing and anti-lasing in a single cavity, Nat. Photonics **10**, 796 (2016).

[51] Y. D. Chong, L. Ge, and A. D. Stone, $\mathcal{PT}$-symmetry breaking and laser-absorber modes in optical scattering systems, Phys. Rev. Lett. **106**, 093902 (2011).

[52] Y. Sun, W. Tan, H.-q. Li, J. Li, and H. Chen, Experimental demonstration of a coherent perfect absorber with PT phase transition, Phys. Rev. Lett. **112**, 143903 (2014).

[53] Y. Aurégan and V. Pagneux, $\mathcal{PT}$-symmetric scattering in flow duct acoustics, Phys. Rev. Lett. **118**, 174301 (2017).

[54] B. Wang, X. Jia, X.-H. Lu, and H. Xiong, $\mathcal{PT}$-symmetric magnon laser in cavity optomagnonics, Phys. Rev. A **105**, 053705 (2022).

[55] Z.-Y. Wang, X.-W. He, X. Han, H.-F. Wang, and S. Zhang, Nonreciprocal $\mathcal{PT}$-symmetric magnon laser in spinning cavity optomagnonics, Opt. Express **32**, 4987 (2024).

[56] Z.-Q. Wang, Z.-Y. Wang, Y.-P. Wang, and J. Q. You, Single-mode magnon-polariton lasing and amplification controlled by dissipative coupling, Phys. Rev. Lett. **135**, 186704 (2025).

[57] J. Qian, Q. Hong, Z.-Y. Wang, W.-X. Wu, Y. Yang, C.-M. Hu, J.-Q. You, and Y.-P. Wang, Unidirectional perfect absorption induced by chiral coupling in spin-momentum locked waveguide magnonics, Nat. Commun. **16**, 8100 (2025).

[58] T. Yu, H. Wang, M. A. Sentef, H. Yu, and G. E. W. Bauer, Magnon trap by chiral spin pumping, Phys. Rev. B **102**, 054429 (2020).

[59] J. W. Rao, P. C. Xu, Y. S. Gui, Y. P. Wang, Y. Yang, B. Yao, J. Dietrich, G. E. Bridges, X. L. Fan, D. S. Xue, and C.-M. Hu, Interferometric control of magnon-induced nearly perfect absorption in cavity magnonics, Nat. Commun. **12**, 1933 (2021).

[60] S. L. Vysotskii, A. V. Sadovnikov, G. M. Dudko, A. V. Kozhevnikov, Y. V. Khivintsev, V. K. Sakharov, N. N. Novitskii, A. I. Stognij, and Y. A. Filimonov, Spin-waves generation at the thickness step of yttrium iron garnet film, Appl. Phys. Lett. **117**, 102403 (2020).

[61] K. Matsumoto, T. Brächer, P. Pirro, T. Fischer, D. Bozhko, M. Geilen, F. Heussner, T. Meyer, B. Hillebrands, and T. Satoh, Optical determination of the exchange stiffness constant in an iron garnet, Jpn. J. Appl. Phys. **57**, 070308 (2018).

[62] C. Dubs, O. Surzhenko, R. Linke, A. Danilewsky, U. Brückner, and J. Dellith, Sub-micrometer yttrium iron garnet LPE films with low ferromagnetic resonance losses, J. Phys. D Appl. Phys. **50**, 204005 (2017).

[63] S. Klingler, A. V. Chumak, T. Mewes, B. Khodadadi, C. Mewes, C. Dubs, O. Surzhenko, B. Hillebrands, and A. Conca, Measurements of the exchange stiffness of YIG films using broadband ferromagnetic resonance techniques, J. Phys. D Appl. Phys. **48**, 015001 (2015).

[64] P. Pirro, T. Brächer, A. V. Chumak, B. Lägel, C. Dubs, O. Surzhenko, P. Görnert, B. Leven, and B. Hillebrands, Spin-wave excitation and propagation in microstructured waveguides of yttrium iron garnet/Pt bilayers, Appl. Phys. Lett. **104**, 012402 (2014).

[65] See Supplemental Material at http://link.aps.org/supplemental/10.1103/21ts-5d39 for nonlinear effect discussion, the Bragg point tuning by period length, magnon lasing in ring geometry, and magnon lasing and antilasing in antiferromagnets, which includes Refs. [66–69].

[66] R. Cheng, D. Xiao, and A. Brataas, Terahertz antiferromagnetic spin Hall nano-oscillator, Phys. Rev. Lett. **116**, 207603 (2016).

[67] O. Johansen, H. Skarsvåg, and A. Brataas, Spin-transfer antiferromagnetic resonance, Phys. Rev. B **97**, 054423 (2018).

[68] V. Baltz, A. Manchon, M. Tsoi, T. Moriyama, T. Ono, and Y. Tserkovnyak, Antiferromagnetic spintronics, Rev. Mod. Phys. **90**, 015005 (2018).

[69] X.-g. Wang, Y.-Z. Nie, L. Chotorlishvili, Q.-l. Xia, J. Berakdar, and G.-h. Guo, Electron-magnon spin conversion and magnonic spin pumping in an antiferromagnet/heavy metal heterostructure, Phys. Rev. B **103**, 064404 (2021).

[70] X.-g. Wang, T.-x. Lu, G.-h. Guo, J. Berakdar, and H. Jing, Zenodo, 10.5281/zenodo.17623011 (2025).